

Generalised quasi-linear approximation of the HMRI

Adam Child¹†, Rainer Hollerbach¹, Brad Marston² and Steven Tobias¹

¹Department of Mathematics, University of Leeds, Leeds, LS2 9JT, UK

²Department of Physics, Box 1843, Brown University, Providence, RI 02912, USA

(Received xx; revised xx; accepted xx)

Motivated by recent advances in Direct Statistical Simulation (DSS) of astrophysical phenomena such as out of equilibrium jets, we perform a Direct Numerical Simulation (DNS) of the helical magnetorotational instability (HMRI) under the generalised quasilinear approximation (GQL). This approximation generalises the quasilinear approximation (QL) to include the self-consistent interaction of large-scale modes, interpolating between fully nonlinear DNS and QL DNS whilst still remaining formally linear in the small scales. In this paper we address whether GQL can more accurately describe low-order statistics of axisymmetric HMRI when compared with QL by performing DNS under various degrees of GQL approximation. We utilise various diagnostics, such as energy spectra in addition to first and second cumulants, for calculations performed for a range of Reynolds and Hartmann numbers (describing rotation and imposed magnetic field strength respectively). We find that GQL performs significantly better than QL in describing the statistics of the HMRI even when relatively few large-scale modes are kept in the formalism. We conclude that DSS based on GQL (GCE2) will be significantly more accurate than that based on QL (CE2).

1. Introduction

The magnetorotational instability (MRI) (Velikhov 1959) is one of the most important processes in modern astrophysics, thought to be responsible for the outward transport of angular momentum in magnetised accretion disks (Balbus & Hawley 1991), and has been the subject of numerous publications in recent years (see the review by Julien & Knobloch (2010)). It is driven by the interaction of large scale Keplerian rotation and mean magnetic fields, and the nonlinear saturation of the instability can lead to turbulent dynamics and efficient angular momentum transport. The presence of an axial magnetic field enables the instability to proceed for fluids with angular momentum profiles that increase with radius; for the same configurations hydrodynamic flows are stable via the Rayleigh criterion.

Direct numerical simulations of this instability (Suzuki & Inutsuka 2014; Bai & Stone 2014; Meheut *et al.* 2015; Gressel & Pessah 2015), though illuminating for the underlying physics, are performed at parameter values that are far from those pertaining to astrophysical disks. For this reason, approaches other than direct solution of the equations have been brought to bear on this problem. The first of these is the utilisation of laboratory experiments in parameter regimes that may not be accessible to numerical simulations. This approach has revealed much about the interaction of rotating fluids, turbulence and magnetic fields as described below, but its direct applicability to the

† Email address for correspondence: mm08ac@leeds.ac.uk

problem of angular momentum transport in disks remains problematic. The second strategy is to utilise Direct Statistical Simulation (DSS) for astrophysical flows (Tobias *et al.* 2011), where the statistics of such flows are obtained directly rather than emerging from averaging of the dynamics from DNS.

As noted above, an important tool to understand such an instability is laboratory experiments. The first of these, by Rüdiger & Zhang (2001) and Ji *et al.* (2001) simultaneously but independently, proposed an experimental set-up with a liquid metal in a cylindrical Taylor-Couette geometry with an imposed axial magnetic field. Instability occurs when the non-dimensional magnetic Reynolds number $\text{Rm} = \Omega_i r_i^2 / \eta \geq O(10)$. Together with the fact that liquid metals have magnetic Prandtl number $\text{Pm} \sim O(10^{-6})$, this translates into a hydrodynamic Reynolds number $\text{Re} = \text{Rm}/\text{Pm} \geq O(10^7)$. Such large values present severe technical difficulties (Schartman *et al.* 2009), especially when it comes to conditions at the end-plates, which have a strong tendency to dominate the flow (Hollerbach & Fournier 2004; Avila 2012; Gissinger *et al.* 2012). As a result, this ‘classical’ set-up has not yet succeeded in obtaining the standard MRI (SMRI) – although the Princeton MRI experiment has yielded many other interesting results (Nornberg *et al.* 2010; Roach *et al.* 2012). Very recently it has also been suggested (Flanagan *et al.* 2015) that the SMRI could be obtained using plasma rather than liquid metal.

Alternatively, Hollerbach & Rüdiger (2005) suggested adding an azimuthal field $B_\phi \sim r^{-1}$, imposed by an electric current running along the central axis of the cylinders. This has a surprisingly large influence on the onset of instability, switching the criterion from $\text{Rm} \geq O(10)$ to $\text{Re} \geq O(10^3)$ – that is, reducing the critical Reynolds number by some four orders of magnitude. Despite this dramatic reduction, and indeed fundamentally different scaling with Pm , this new instability, now known as the helical MRI (HMRI), is continuously connected to the SMRI (although a number of subtleties are involved (Kirillov & Stefani 2010; Kirillov *et al.* 2014)). Following its theoretical prediction, the HMRI was quickly observed in a series of experiments in the PROMISE facility (see (Stefani *et al.* 2009) and earlier references therein). The HMRI also continues to be the subject of further theoretical analysis (Liu *et al.* 2006; Priede *et al.* 2007; Priede 2011).

The main purpose of this paper, however, is to determine the regime of applicability of the GQL approximation for a system of wall-bounded, electrically conducting flows. The HMRI is an excellent system to elucidate the strengths and weaknesses of this approach as it shows turbulent dynamics even in its axisymmetric configuration described above. The GQL representation has been examined in the context of two-dimensional driven turbulence on a spherical surface and β -plane and shown to be more effective than the regular QL approximation in reproducing both the dynamics and statistics of these flows away from equilibrium (Marston *et al.* 2016). The importance of establishing the regime of applicability of various approximations arises owing to their use in deriving statistical theories.

As noted by Tobias *et al.* (2011), the enormous range of spatial and temporal scales present in many astrophysical phenomena poses a problem for DNS in that each scale must be properly resolved; this is unlikely, even on today’s powerful parallel computers — and indeed those of the foreseeable future. The problem is that in most astrophysical applications, the large-scale dynamics are influenced by, and in turn influence, the small-scale interactions.

A complementary approach, that has been afforded much attention recently is that of Direct Statistical Simulation (DSS), in which the low-order statistics are obtained directly from a hierarchy of cumulant equations, and a closure is applied to this hierarchy in order to provide tractable calculations. DSS has a number of advantages over DNS, chiefly that the statistics vary slowly in time and are smoother in space and can be explored via the

evolution of relatively few modes on a slow manifold. There have been a number of examples of Direct Statistical Simulation in recent works, most notably involving various planetary jets; Tobias *et al.* (2011) derived a formulation for flow on rotating spherical surface and compared with the DNS solutions showing considerable accuracy. Indeed, DSS is shown to be useful in analysing the underlying physics of flows in that it in this case demonstrates that jets may be formed without an inverse cascade. Moreover, quasilinear statistical framework has allowed Squire & Bhattacharjee (2015) to probe the MRI dynamo in a shearing box in ways inaccessible in conventional DNS. All of the above investigations used the most simple form of DSS (known as CE2) — this approximation is the statistical representation of the quasilinear approximation (QL). At this quasilinear level of approximation DSS is formally equivalent to the Stochastic Structural Stability Theory (SSST or S3T) of Farrell, Ioannou and collaborators (Farrell & Ioannou 2007; Farrell & Ioannou 2008; Constantinou *et al.* 2013), which has been extensively used to model a number of physical systems and can be justified for systems near equilibrium for which there is a separation of timescales (Bouchet *et al.* 2013).

Of course, this is not to imply that quasilinear DSS (i.e. CE2) is universally applicable; there are a number of examples of inconsistencies with fully nonlinear DNS (NL DNS), evident for example in out-of-equilibrium jets studied with DSS for a number of parameter combinations. Far from equilibrium, CE2 ceases to be an adequate representation of the system, as shown by Tobias & Marston (2013). In that paper it was demonstrated that when the system was in statistical equilibrium and thus dominated by strong jets, CE2 does in fact do a good job of reproducing both the number and strength of jets in the system. However, the further away from equilibrium, the worse CE2 is seen to perform, resulting in both inaccurate jet strengths and inaccurate numbers of jets (see also Srinivasan & Young (2012)). Two options have been suggested to remedy the situation. The first is to include eddy-eddy scattering in the truncation. This leads to the CE3 (or CE2.5) approximation, which has been shown to improve performance of DSS away from equilibrium (Marston *et al.* 2014).

A second possibility is to generalise the quasilinear approximation (Marston *et al.* 2016) and derive a corresponding statistical theory (GCE2). We explore the accuracy of such direct statistical simulation of the HMRI at GCE2 by performing a series of generalised quasilinear DNS (QL DNS) in the inductionless limit. First we formulate the model and give details of the methods utilised for DNS. We continue by defining the GQL approximation and compare its efficacy with that of QL theory by examining how well it reproduces a number of diagnostic quantities, such as the energy spectra and first and second cumulants of the flow. We conclude by briefly discussing the implications of our results to possible statistical simulations.

2. Formulation and Numerical Method

We consider axisymmetric cylindrical Taylor-Couette flow, with radii and angular velocities at the inner and outer cylinders given by r_i, r_o and Ω_i and Ω_o respectively. We set $r_i/r_o = 0.5$ to coincide with the aspect ratio of the PROMISE experiment. Unlike an experiment though, with its inevitable end-plates, we take the cylinders to be axially periodic with a basic periodicity of 40 times the gap-width. This is sufficiently long to allow turbulent structures to develop in the axial direction; it is the dynamics and interactions of these structures that we then wish to explore in this work.

The flow and magnetic field are described by the Navier-Stokes and induction equa-

tions,

$$\text{Re} \frac{\partial \mathbf{U}}{\partial t} - \nabla^2 \mathbf{U} = -\nabla p - \text{Re} \mathbf{U} \cdot \nabla \mathbf{U} + \text{Ha}^2 \text{Rm}^{-1} (\nabla \times \mathbf{B}) \times \mathbf{B}, \quad (2.1)$$

$$\frac{\partial \mathbf{B}}{\partial t} = \nabla \times (\mathbf{U} \times \mathbf{B}) + \text{Rm}^{-1} \nabla^2 \mathbf{B}, \quad (2.2)$$

where we have non-dimensionalised as follows: we scale lengths with the gap-width $(r_o - r_i)\hat{r}$, time on the rotational time-scale $t = \Omega_i^{-1}\hat{t}$, U proportional to length over time, $U = (r_o - r_i)\Omega_i\hat{U}$, and $B = B_z\hat{B}$, with B_z the strength of the imposed axial magnetic field. The nondimensional quantities

$$\text{Rm} = (r_o - r_i)\Omega_i/\eta, \quad \text{Re} = (r_o - r_i)\Omega_i/\nu, \quad \text{Ha} = B_z(r_o - r_i)/\sqrt{\eta\nu\mu_0\rho} \quad (2.3)$$

are the magnetic and hydrodynamic Reynolds numbers and the Hartmann number respectively.

As noted above, for the SMRI it is crucial that Rm be retained, and exceed $O(10)$. In contrast, the HMRI continues to exist even in the so-called inductionless limit $\text{Rm} \rightarrow 0$. Splitting the magnetic field into imposed and induced fields as $\mathbf{B} = \mathbf{B}_0 + \text{Rm} \mathbf{b}$ and then letting $\text{Rm} \rightarrow 0$ yields

$$\text{Re} \frac{\partial \mathbf{U}}{\partial t} - \nabla^2 \mathbf{U} = -\nabla p - \text{Re} \mathbf{U} \cdot \nabla \mathbf{U} + \text{Ha}^2 (\nabla \times \mathbf{b}) \times \mathbf{B}_0, \quad (2.4)$$

$$0 = \nabla^2 \mathbf{b} + \nabla \times (\mathbf{U} \times \mathbf{B}_0). \quad (2.5)$$

Note also that in this limit the only nonlinearity arises from the inertial term $\mathbf{U} \cdot \nabla \mathbf{U}$.

The imposed field is given by $\mathbf{B}_0 = \mathbf{e}_z + \beta r^{-1} \mathbf{e}_\phi$; the HMRI operates when $\beta \geq O(1)$ (Hollerbach & Rüdiger 2005). The rotation ratio is fixed at $\Omega_o/\Omega_i = 0.27$, slightly beyond the Rayleigh value 0.25. That is, for $\Omega_o/\Omega_i < 0.25$ one would obtain purely hydrodynamic instabilities, which we are not interested in here, but for $\Omega_o/\Omega_i > 0.25$ one obtains only the HMRI, for appropriate values of the three governing parameters Re , Ha , and β .

The boundary conditions on \mathbf{U} are no-slip, as they must be for any Couette flow. For \mathbf{b} the HMRI exists in much the same form for either insulating (Hollerbach & Rüdiger 2005) or perfectly conducting (Rüdiger *et al.* 2006) boundaries. Since Fig. 2 of Rüdiger *et al.* (2006) mapped out a particularly thorough set of linear onset curves for perfectly conducting boundary conditions we will here consider only perfectly conducting boundaries.

Because the HMRI is an intrinsically axisymmetric phenomenon (just like the SMRI), we restrict attention to axisymmetric solutions, and further decompose as

$$\mathbf{U} = v \mathbf{e}_\phi + \nabla \times (\psi \mathbf{e}_\phi), \quad \mathbf{b} = a \mathbf{e}_\phi + \nabla \times (b \mathbf{e}_\phi), \quad (2.6)$$

thereby automatically satisfying $\nabla \cdot \mathbf{U} = \nabla \cdot \mathbf{b} = 0$.

The full details of the numerical solution for v , ψ , a and b are presented in Hollerbach (2008). Here we merely note that the radial structure is expanded in 50 Chebyshev polynomials, and the axial structure in 600 Fourier modes of the form $\exp(i\kappa z)$, where $\kappa = 2\pi k/z_0$, with $z_0 = 40$ the imposed basic periodicity. The essence of the GQL again is to study interactions between different Fourier modes, so such a decomposition is convenient both numerically and theoretically.

2.1. Generalised quasilinear approximation

In this section we outline how to apply the generalised quasilinear approximation introduced by Marston *et al.* (2016) to this axisymmetric HMRI system. For simplicity, let us consider the velocity \mathbf{U} , though similar considerations are applied to the perturbed

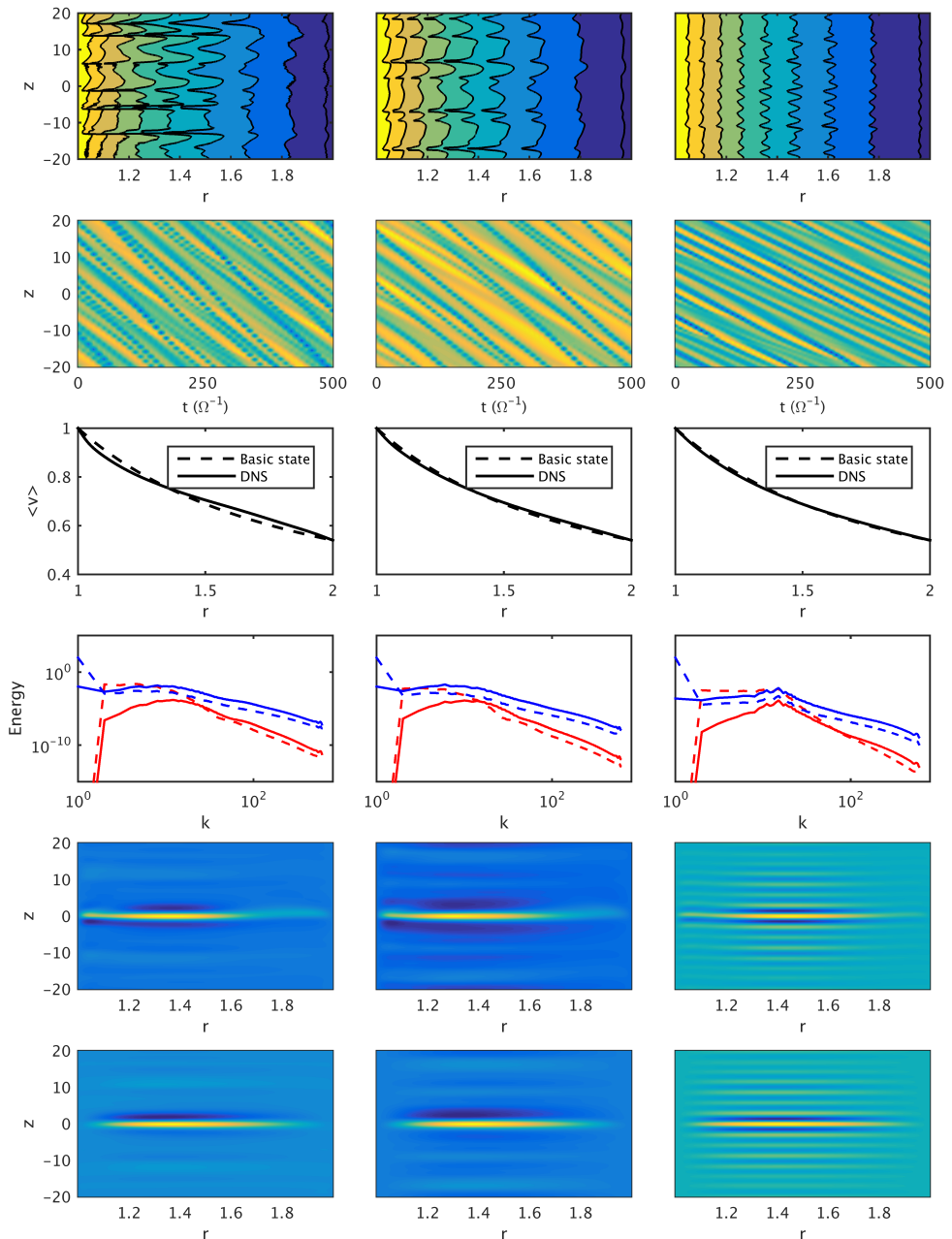


Figure 1: Row: i) Contour snapshots of the azimuthal velocity in a radial cross section; ii) Hovmöller plots of ψ as a function of z and time; iii) Mean azimuthal flow (first cumulant) as a function of r ; iv) Vertical energy spectra for the magnetic field (red) and velocity (blue) with poloidal components (solid) and toroidal components (dashed); v) Second cumulants $\langle v'v' \rangle$; vi) Second cumulants $\langle v'\psi' \rangle$. Shown on the left is $\beta = 5$, $\text{Ha} = 16$, in the centre is $\beta = 2.5$, $\text{Ha} = 16$, and on the right is $\beta = 10$, $\text{Ha} = 8$, each for $\text{Re} = 10^4$.

magnetic field \mathbf{b} . In general the fields may be split via a standard Reynolds decomposition into mean and fluctuation (eddy) components, for example for the azimuthal velocity

$$v = \bar{v} + v' \quad (2.7)$$

where overbar denotes a mean and prime denotes fluctuations about that mean. In previous papers the averaging procedure has involved taking a zonal mean, but in this axisymmetric geometry a natural definition of the mean is that part that is independent of the z -coordinate (i.e. the $\kappa = 0$ mode). This standard definition for the mean and fluctuations (eddies) then naturally leads to the quasilinear approximation. In this approximation certain mode interactions are discarded from the dynamics. In particular whilst mean/eddy \rightarrow eddy and eddy/eddy \rightarrow mean interactions are kept, eddy/eddy \rightarrow eddy interactions are discarded. In this quasilinear approximation therefore only nonlocal (in wavenumber) elements of cascades or inverse cascades are possible (Tobias *et al.* 2011)

A similar decomposition is used for GQL. However here the velocity is decomposed into large and small scale modes, where large and small scale are defined by the spectral wavenumber. That is we set

$$v(r, z) = \sum_{k=0}^{\Lambda} v_{lk}(r) e^{i\kappa z} + \sum_{k=\Lambda+1}^{N_k} v_{hk}(r) e^{i\kappa z}, \quad (2.8)$$

where the v_l and v_h are the large scale (denoted l for ‘low’ modes) and smaller scale (denoted h for ‘high’ modes) respectively, and Λ is the mode cut-off point between the two. It is clear then that when $\Lambda = 0$ this expansion is the same as that for QL given in equation (2.7). Hence the GQL formalism reverts to QL when $\Lambda = 0$ as noted by Marston *et al.* (2016)

When $\Lambda \neq 0$ and the Generalised Quasilinear approximation differs from QL, the triad interactions that are retained and discarded are selected so as to satisfy the relevant conservation laws and enable closure (Marston *et al.* 2016). Briefly this involves retaining low/low \rightarrow low, high/high \rightarrow low and low/high \rightarrow high interactions and discarding all others. Again retaining this set of interactions is consistent with QL when $\Lambda = 0$. Furthermore as $\Lambda \rightarrow \infty$ the system consists solely of low modes and is formally the same as Direct Numerical Simulation. The aim of this paper is to determine how well GQL performs in reproducing the NL DNS results as Λ is varied; clearly if it is able to do so for relatively small Λ then this is extremely encouraging for producing Direct Statistical Simulation based on the GQL approximation.

3. Results

3.1. Means of Comparison: Outputs of Interest

As DSS is a statistical theory, we shall evaluate the GQL approximation by accumulating statistics using QL DNS and testing how well GQL reproduces the statistics of the HMRI (Marston *et al.* (2016) evaluated both the statistics and the dynamics for the problem of the driving of zonal jets). To that end we shall calculate average vertical spectra of the flow and magnetic field as well as the first and second cumulants for the flow. The first cumulant is the mean over z and time as a function of r defined as

$$c_\psi(r) = \langle \psi(r, z, t) \rangle, \quad c_v(r) = \langle v(r, z, t) \rangle, \quad (3.1)$$

where angled brackets indicate averaging over z and t . the second cumulants yield information about the (non-local) fluctuation/fluctuation interactions and are defined

as

$$c_{\psi\psi}(r_1, r_2, z_1, z_2) = \langle \psi'(r_1, z_1, t) \psi'(r_2, z_2, t) \rangle, \quad (3.2)$$

$$c_{vv}(r_1, r_2, z_1, z_2) = \langle v'(r_1, z_1, t) v'(r_2, z_2, t) \rangle, \quad (3.3)$$

$$c_{v\psi}(r_1, r_2, z_1, z_2) = \langle v'(r_1, z_1, t) \psi'(r_2, z_2, t) \rangle. \quad (3.4)$$

The second cumulant can then be expressed as, for example

$$c_{\psi\psi}(r_1, r_2, \xi) = \int \int \psi'(r_1, z_1) \psi'(r_2, z_1 + \xi) dz_1 dt \quad (3.5)$$

where $\xi = z_2 - z_1$. In this paper, we choose r_1 to be the point halfway between the two cylinders.

3.2. Parameter Choice and Initialisation

The generalised quasilinear approximation is straightforward to implement in the pseudo-spectral timestepping code – the various triad interactions discussed by Marston *et al.* (2016) can be easily isolated in spectral space and discarded or retained as required. We performed a number of simulations under various different parameter regimes for a number of truncations of the large scale modes Λ .

We initialise each simulation using the following procedure. For each parameter set we run a fully turbulent NL DNS solution until it reaches a statistically stationary state. It is this state that we use as initial conditions for runs at the same parameter values but with different cut-offs for the GQL approximation. We note that the same results are obtained if the GQL calculations are started from rest — though these take longer to equilibrate. For each parameter set we evolve $\Lambda = 0$ (corresponding directly to the QL expansion) and we also examine $\Lambda = 1, 2, 3, 6$ and $\Lambda = 20$. We evolve each of the equations using a timestep $dt = 5 \times 10^{-3}$, and run each simulation for a minimum of 8×10^4 timesteps to make sure that the solutions reached are statistically steady. Any averages (over time) are then calculated using 300 equally spaced (in time) solutions, commencing from the 200000th step.

We also give here some note about the rationale for our choice of model parameters — care has to be taken to make sure that Re is sufficiently above Re_c , the critical Reynolds number. Intuitively, one might expect that the supercriticality of the system as measured by $(\text{Re} - \text{Re}_c)$ will have bearing on the effectiveness of the QGL approximations, and so we choose to examine a number of different parameter sets. Based on Fig. 2 of (Rüdiger *et al.* 2006), we choose to focus on three specific choices; $\beta = 5$, $\text{Ha} = 16$, $\beta = 2.5$, $\text{Ha} = 16$ and $\beta = 10$, $\text{Ha} = 8$, each for $\text{Re} = 5000, 7000$ and 10000 . These choices ensure that the flow is sufficiently supercritical to generate a turbulent state. Of the three parameters sets, $\beta = 5$, $\text{Ha} = 16$ has $\text{Re}_c \approx 1000$, and is the most supercritical, and $\beta = 2.5$, $\text{Ha} = 16$ has a slightly higher $\text{Re}_c \approx 1500$, and thus will give insight into how the GQL approximation holds for less turbulent flows. The point $\beta = 10$, $\text{Ha} = 8$ is more interesting in that, even though $\text{Re}_c < 1000$, on the aforementioned figure the contours of Re_c are closely bunched together. That is, the flow would be viewed as being highly supercritical when the Reynolds parameter alone is examined, but close to marginal stability in terms of the magnetic field parameters. This is of particular interest in that it suggests that this parameter set may be only weakly nonlinear, for which we would expect even the standard QL approximation to give an accurate reproduction of the NL DNS. We claim that these three points and Re values sufficiently encapsulate the properties of the GQL approximation; simulations for other parameters yield qualitatively similar results.

3.3. NL DNS

We begin by describing the behaviour of the system for NL DNS of the HMRI. In figure 1, we show plots of various quantities – contours of the azimuthal velocity, Hovmöller diagrams, mean azimuthal flows (first cumulants), energy spectra, and second cumulants – for each parameter combination at the highest value of the Reynolds number $\text{Re} = 10000$. As seen in row 1 of figure 1, different parameter choices lead to varying degrees of turbulence, with $\beta = 5$, $\text{Ha} = 16$ (first column) being the strongest, and $\beta = 10$, $\text{Ha} = 8$ (last column) – that which we suspect is only weakly nonlinear – being the weakest.

The HMRI is known to be a unidirectionally travelling wave at onset (Hollerbach & Rüdiger 2005; Rüdiger *et al.* 2006), due to the $\pm z$ symmetry-breaking caused by an imposed field having both axial and azimuthal components (Knobloch 1996). This drifting nature is conveniently visualised by presenting a number of Hovmöller plots of $\psi(t, z)$ for a given radius, which allow the identification of the location of Taylor vortices. The streamfunction ψ undergoes a reversal in sign when transitioning from one Taylor vortex to another. Therefore, simply plotting the sign of ψ is equivalent to tracking the position of the vortices over time. It can be seen clearly that in DNS the vortices propagate downward in the axial direction as a travelling wave. Also apparent on these plots is the number of dislocations present in the flow; these are an effective measure of the strength of turbulence. It can be seen that in general, as expected, the number of dislocations decreases as Re_c increases for fixed Re , i.e. as the flow becomes less supercritical. However, at the point identified as only weakly nonlinear few of these nonlinear dislocations occur. The mean azimuthal flows shown in the third row demonstrate the change from the basic state. As expected the role of turbulence is to decrease the gradient of the mean azimuthal flow (removing the source of instability). For the more turbulent flows this change is more significant whilst for the less supercritical flows the departure from the mean state is much less pronounced as expected.

Turning our attention to the energy spectra, for which we plot the energy of both the toroidal and poloidal components of the magnetic field (in red) and velocity (in blue), we may note that regardless of the parameter regime, these are qualitatively very similar. The magnetic energy is smaller than that for the kinetic energy and has a steeper spectrum. In the weakly nonlinear case the energy peaks at a modenumber $k \approx 13$, which is similar to the linear mode of maximum growth-rate. The energy spectra for $\text{Re} = 7000$ and $\text{Re} = 5000$ have similar characteristics to these plots. The second cumulants $\langle v'v' \rangle$ and $\langle v'\psi' \rangle$ are very much localised in the axial direction, though there is strong radial correlation with the midpoint in radius. The axial localisation is a reflection of the flat energy spectra for the low modes, which leads to this δ -function-like axial structure in the second cumulants. For the weaker turbulence (third column), the cumulants are different in that a periodic axial correlation is now apparent, such that flow at a point is correlated not only in the radial direction, but also periodically in each direction along the axis. A wavenumber of $k \approx 13$ in the second cumulants is observed, which corresponds to the peak observed in the energy spectrum.

These results will be used in the next section as benchmarks to evaluate the effectiveness of the GQL approximation at various truncations.

3.4. GQL DNS

3.4.1. Weak turbulence: $\beta = 10$ $\text{Ha} = 8$

We start by examining the effectiveness of GQL DNS in comparison with QL DNS for the weak turbulence case $\beta = 10$, $\text{Ha} = 8$, $\text{Re} = 10000$ (for which the DNS results are shown in the third column of Figure 1). It is to be expected that the QL approximation

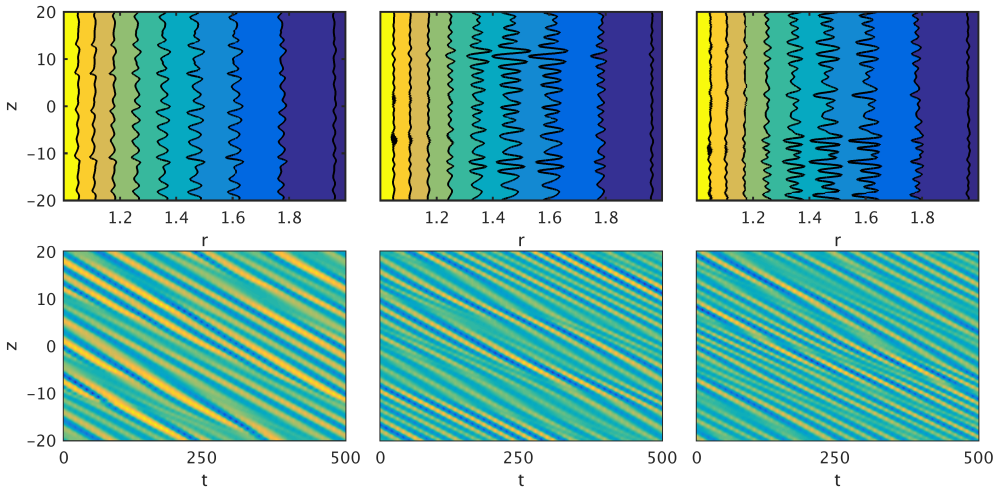


Figure 2: Snapshot contour plots of u_ϕ (top) and Hovmöller plots (bottom) for $\beta = 10$, $\text{Ha} = 8$, $\text{Re} = 10^4$. Shown on the left is the NL DNS, in the middle is $\Lambda = 0$, and on the right is $\Lambda = 2$.

will most likely have the greatest success in this parameter regime, as nonlinearities have smaller influence on the instability; recall QL is an exact representation of the dynamics in the formally weakly nonlinear regime. We can see on comparing the Hovmöller plots (figure 2) that this expectation is correct; there are few dislocations in the NL DNS, meaning that even $\Lambda = 0$ is an accurate approximation.

We can see from the first cumulants (figure 3(a)) that the various Λ approximations are near indistinguishable from the NL DNS profile. Even the quasilinear $\Lambda = 0$ gives an excellent approximation to the full solution. Indeed, for the first cumulants there is little advantage in using a GQL approximation over a QL approximation. Again for such a laminar solution this is perhaps to be expected.

Moreover, even $\Lambda = 0$ reproduces axial structure the second cumulants fairly well at $\text{Re} = 10000$ (figure 4). The axial wavelength and magnitudes are marginally inaccurate and the radial correlation is focussed at the mid-point instead of across the full gap width, however they are surprisingly good for such a crude approximation to the non-linearity. Interestingly, the correlation structure is still finer than that of the NL DNS, due to the peak at $k \approx 20$ that is present in all QL solutions. This structure becomes finer as Λ is increased, though the magnitudes of the spurious correlations decrease. However, we comment that $\Lambda = 0$ does not give universally adequate approximations even in this weakly turbulent case. If we examine $\text{Re} = 5000$ (not shown), the cumulant structure is much less accurate; it is not until $\Lambda = 2$, that the axial cumulant structure resembles the NL DNS case. So, whilst for much of this weakly nonlinear parameter regime the standard QL approximation produced adequate first and second cumulants, this can not be guaranteed for all Re – the $\Lambda = 2$ GQL is required to further guarantee this level of accuracy.

3.4.2. Strong turbulence: $\beta = 5$ $\text{Ha} = 16$

We next examine the GQL approximation at the set of parameters $\beta = 5$, $\text{Ha} = 16$, for which we plot the same diagnostic quantities as for NL DNS. From figure 5, it is clear that the azimuthal velocity profile is quite different in the $\Lambda = 0$ case to that for NL DNS, with

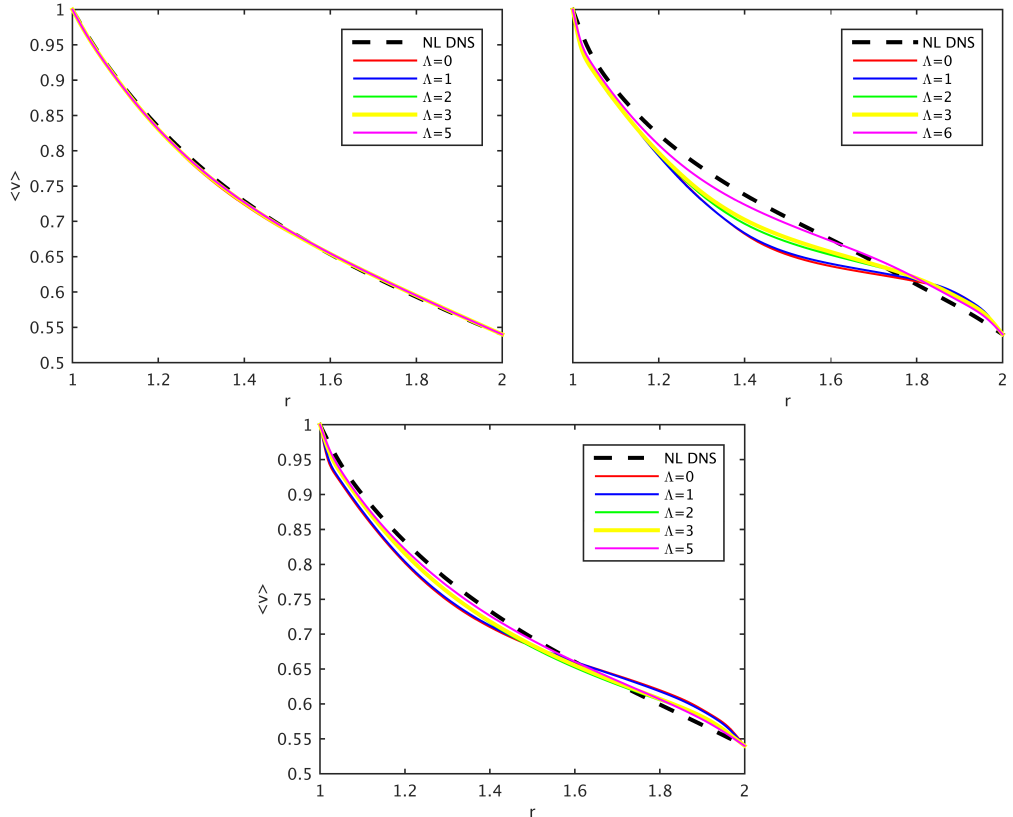


Figure 3: First cumulants $\langle v \rangle$ for $\beta = 10$ Ha = 8 (top left), $\beta = 5$ Ha = 16 (top right) and $\beta = 2.5$ Ha = 16 (bottom). Note that for $\beta = 10$ Ha = 16, as the flow is only weakly nonlinear the NL DNS and GQL DNS profiles are near indistinguishable.

the QL approximation failing to reproduce dislocations. Importantly however, we note that the Hovmöller plots show that the travelling wave property is preserved, even by the standard $\Lambda = 0$ QL approximation. The wavelength, though difficult to measure due to dislocations, can be seen to be within an acceptable range of the NL DNS. Note that if the $\Lambda = 2$ GQL approximation is taken, even the nonlinear dislocations are reproduced; a significant improvement over $\Lambda = 0$.

Additionally, we compare the energy spectrum to that of the NL DNS (figure 6). It should be noted that agreement in the lower modes of the spectrum is the most important for the evaluation of the approximation. We observe that the energy in the GQL approximation is located primarily in the lower modes, which peak higher than in the original NL DNS case. Because energy is not being transferred by nonlinear processes the higher modes contain much less, if any, energy and the turbulent cascade is no longer present.

The most striking features in these plots are the strong peaks in the spectra for GQL at $\Lambda = 0$ and $\Lambda = 1$, which correspond to a linear instability and its harmonics. The first peak occurs at a mode number $k = 40$, and the other peaks appear to be the resonance of this at $k = 80$ and $k = 160$. A key question one may ask is whether this is due to the initial condition – recall that we started with a fully turbulent state from which

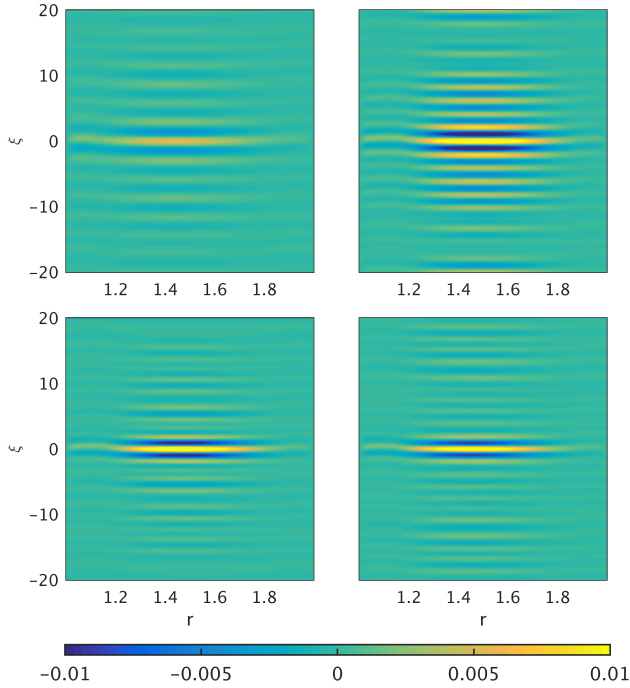


Figure 4: Second cumulants $\langle v'v' \rangle$ at $\beta = 10$ Ha = 8 for NL DNS (top left), QL DNS ($\Lambda = 0$) (top right), and GQL DNS with $\Lambda = 2$ (bottom left), $\Lambda = 3$ (bottom right). Recall that here we choose r_1 to be the point halfway between the two cylinders.

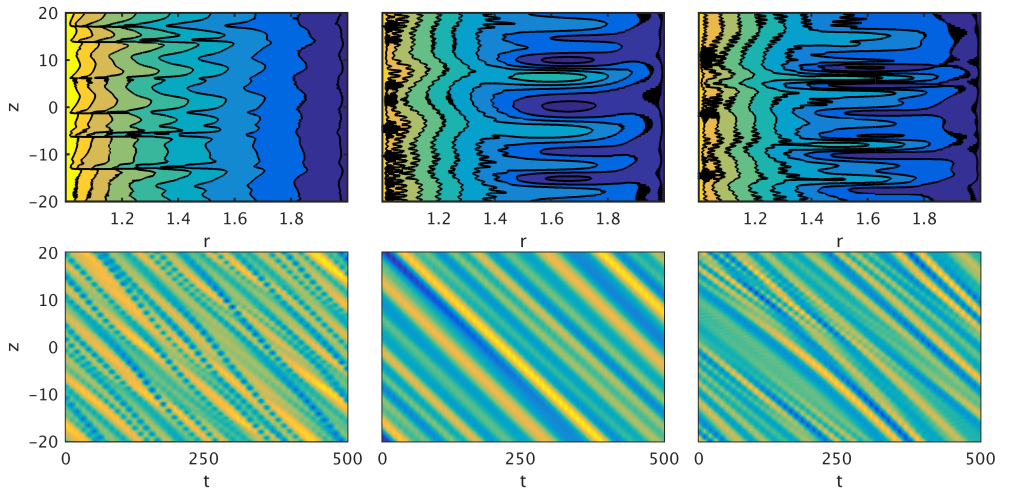


Figure 5: Snapshot contour plots of u_ϕ (top) and Hovmöller plots (bottom) for $\beta = 5$, Ha = 16, Re = 10^4 . Shown on the left is the NL DNS, in the middle is $\Lambda = 0$, and on the right is $\Lambda = 2$.

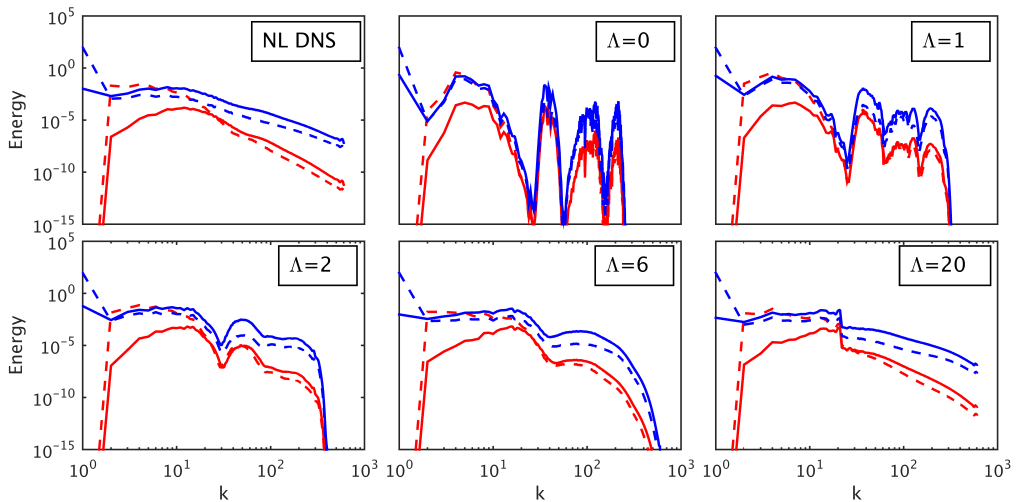


Figure 6: Vertical energy spectra for the various mode truncations at $\beta = 5$, $\text{Ha} = 16$, $\text{Re} = 10000$ with magnetic field (red) and velocity (blue) and with poloidal components (solid) and toroidal components (dashed).

the energy could have decayed away in the upper spectra. As noted earlier, even if the simulations are started from a small perturbation about the basic state these peaks still exist in the spectra, therefore the energy must be transferred outwards to them. For $\Lambda = 1$ we still detect these linear peaks, though due to the increased energy scattering off the low modes some energy has now transferred outwards to the modes between them.

If we turn our attention to $\Lambda = 2$, it can be seen that the energy in higher modes becomes more like that in the NL DNS, even if it does decay at a much greater rate for $k > 200$. The linear instability peak is still present, however it is but a small protrusion above the energy stored in adjacent modes, and for the modes immediately higher than $k = 20$ the spectrum begins to resemble the power law from the NL DNS. The improvement in reproduction of the DNS spectrum over $\Lambda = 0$ is clear, yet it can also be seen that increasing $\Lambda > 2$ does not yield similarly great increases in accuracy ($\Lambda = 6$ produces an almost equivalent spectrum). Interestingly there is a sharp decrease in energy around the mode $k = 20$, which persists even for $\Lambda = 20$, where the rest of the spectra resembles the NL DNS. For this large Λ , we see that the energy is higher than the NL DNS in the modes slightly lower, and lower in the slightly higher modes, whilst virtually identical to the NL DNS otherwise.

If we turn our attention to the first cumulants $\langle v \rangle$ in figure 3, we see that for $\Lambda = 0$ (QL) they deviate approximately 10% from the NL DNS solution. As Λ is increased the cumulants then approach the profile of NL DNS, with a large improvement in agreement shown between $\Lambda = 1$ and $\Lambda = 2$, in agreement with what is seen in the energy spectra. The deviation gets smaller as Re is decreased (not shown) but decreasing Re does not lead to a better approximation; the lower Reynolds number simply means that the cylinder is rotating with lower angular velocity and thus the overall perturbation in the velocity profile is smaller, with the percentage error for QL staying approximately the same.

We also compare plots of the second cumulant, $\langle v'v' \rangle$. Recall we choose to display the cross-correlation with the mid-point of the gap between the cylinders. The choice of Re has a slight influence on the second cumulants though does not significantly alter their

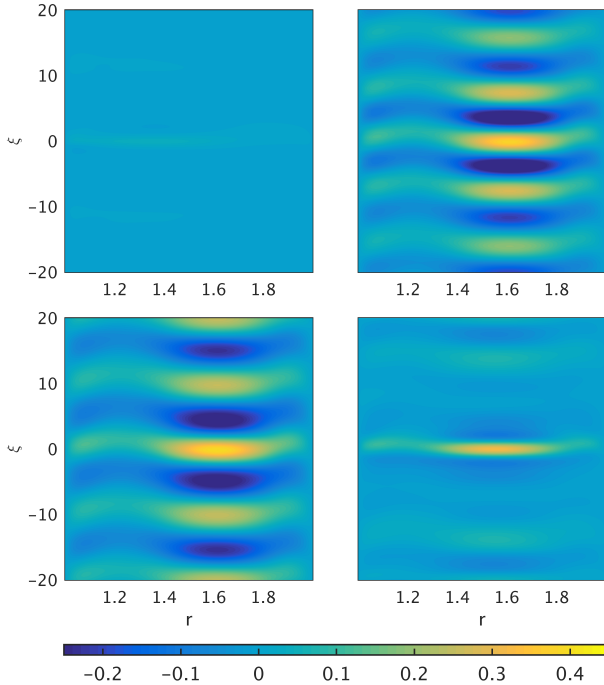


Figure 7: Second cumulants $\langle v'v' \rangle$, as in Figure 4, at a number of mode truncations for the parameter regime $\beta = 5$ $\text{Ha} = 16$, $\text{Re} = 7000$. Shown are; NL DNS (top left), QL DNS ($\Lambda = 0$) (top right), and GQL DNS with $\Lambda = 1$ (bottom left), $\Lambda = 2$ (bottom right).

axial structure. Thus, we choose to examine the case when $\text{Re} = 7000$ to illustrate the behaviour of the second cumulants in the GQL approximation.

It is immediately clear from Figure 7 that the second cumulants for $\Lambda = 0$ and $\Lambda = 1$ are inadequate reproductions of the NL DNS case — for these approximations there is an uncharacteristically large observed axial correlation. Indeed, if we take $\Lambda = 0$ we see that the correlation has a wavenumber of 5, whereas the NL DNS is strongly correlated with one axial location, and is very weakly (or un-) correlated with the rest of the domain. Interestingly, $\Lambda = 1$ has correlation of wavenumber 4, possibly associated with the presence of waves travelling axially (see also Marston *et al.* (2016)). Recall that the localisation of the second cumulant appeared to be associated with the absence of a strong spectral peak. As such, by $\Lambda = 2$ the axial localisation of the second cumulant has been re-established.

We note similar structure in the cross cumulants $\langle v'\psi' \rangle$, which are plotted in figure 8. A similar overcorrelation is seen for $\Lambda = 0$ and $\Lambda = 1$, though v' is out of phase with ψ' . At $\Lambda = 2$ we see that the structure of the NL DNS is regained, with all but the axial midpoint being very weakly correlated. Note how now the radial correlation is much more consistent across the NL DNS and GQL approximations than previous.

3.4.3. $\beta = 2.5$ $\text{Ha} = 16$: moderate turbulence

As mentioned previously, this parameter set is much less turbulent than $\beta = 5$, $\text{Ha} = 16$, with fewer dislocations in the NL DNS. Thus, it can inform us of the effect that Re_c has on the viability of the GQL, in a similar fashion to the reduced Re cases previously. Much like before, it can be found that the fundamental travelling wave property is reproduced

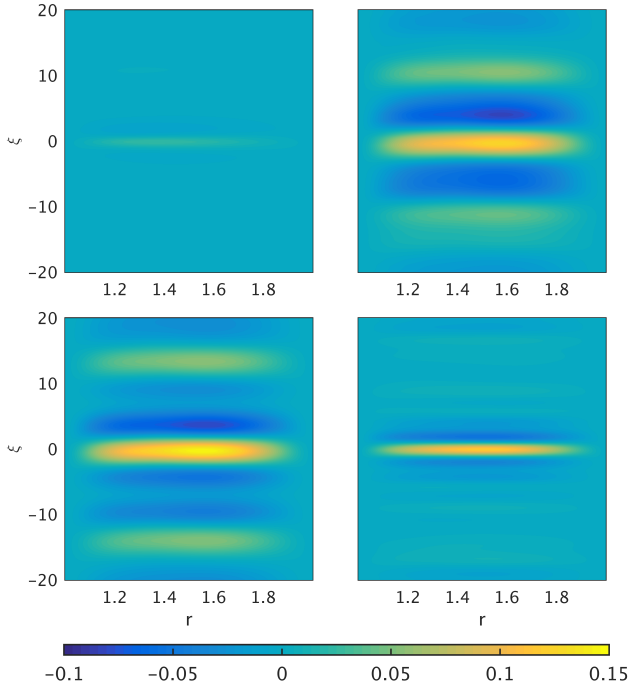


Figure 8: As for Figure 7 but for cross cumulants $\langle v'\psi' \rangle$.

even for $\Lambda = 0$, and it is not until $\Lambda = 2$ that nonlinear nonlinear dislocations are again found in Hovmöller plots.

If we examine the first cumulants in figure 3 we see that they have profiles that are very close to that of the NL DNS, whatever the degree of approximation — though improvement is seen as Λ is increased. We briefly comment that the energy spectra and second cumulants show similar behaviour to those for the strong turbulence case described above, with GQL beginning to yield a good approximation by $\Lambda = 5$. Hence we conclude that even if QL appears to give an adequate approximation on examination of the mean flows, GQL may be required for accurate representation of the fluctuations.

4. Conclusion

In this paper we have extensively examined the effectiveness of the Generalised Quasi-linear Approximation (GQL) for the case of an axisymmetric HMRI for a number of different parameter regimes, with flows varying from weakly to strongly turbulent. Establishing the approximation's effectiveness is important not only for determining which interactions play a key role in the dynamics of the system, but also for determining the minimum ingredient of a statistical theory (such as Direct Statistical Simulation) that is necessary to reproduce the low-order statistics of the system.

For weakly turbulent systems we find no fundamental problems with the possibility of DSS and the HMRI — even for the QL case of $\Lambda = 0$ the travelling wave behaviour is reproduced, even if some of the other properties are of varying degrees of accuracy. However when the system is more turbulent we have found that for the GQL approximation at $\Lambda = 2$, much more accurate results can be obtained, and that increasing Λ

further yields diminishing returns, with a much lesser improvement in accuracy per extra mode included. We have seen that $\Lambda = 2$ gives a much improved spectra compared with $\Lambda = 0$. The various cumulants further reinforce this; $\Lambda = 0$ for the most part yields over-correlated second cumulants, and it is not until $\Lambda = 2$ that the correlation structures properly resemble the NL DNS.

The choice of parameter regime has a knock-on effect in the accuracy of the GQL approximation, with the degree of supercriticality an important factor. However, for the majority of the parameter space the influence that β , Ha , and Re have on the approximations has little effect on the relative accuracy of the different Λ approximations; in each regime it was found that increasing to $\Lambda = 2$ offers a marked improvement over the $\Lambda = 0$ case whilst increasing $\Lambda > 2$ yields much smaller increases in accuracy. Special points, such as the weakly nonlinear $\beta = 10$, $\text{Ha} = 8$ may be approximated to a good degree of accuracy using even the $\Lambda = 0$ approximation. However, these are but a small section of the total parameter space.

This leads us to two main conclusions. Firstly, as the HMRI is the subject of much current research, it may be fruitful to perform direct statistical simulations of the instability. Having shown that using a GQL approximation may yield accurate results, the equivalent cumulant expansion to the $\Lambda = 2$ case may be used to give further insight into the instability.

Secondly, and most importantly, this work shows that for some problems it may be advantageous to use cumulant expansions other than the quasilinear CE2 expansion to conduct direct statistical simulation. As mentioned in the introduction, previous research has shown that DSS via the CE2 expansion (equivalent to $\Lambda = 0$), whilst accurate for problems such as out of equilibria jets, can also prove inaccurate. We have shown that for the HMRI, where taking a standard QL approximation would have been inadequate, even the addition of two more large scale modes in the $\Lambda = 2$ approximation yields markedly more accurate solutions. It is logical to conclude that a similar $\Lambda \geq 2$ cumulant expansion would allow for accurate DSS in other flows, without compromising the computational advantage of DSS over DNS. These results reinforce those of Marston *et al.* (2016) who found that the GQL approximation may yield significant enhancement over QL for the hydrodynamic problem of jet formation on a spherical surface or β -plane.

Finally, we note that while we have here only considered the axisymmetric HMRI, for only slightly larger Hartmann numbers there is also a non-axisymmetric analog, the so-called azimuthal MRI (AMRI). This mode undergoes a similar switch in scaling from Rm to Re as in the SMRI \rightarrow HMRI transition (Hollerbach *et al.* 2010), and has by now also been observed in the PROMISE experiment (Seilmayer *et al.* 2014). 3D numerical modelling of these modes is only just beginning (Guseva *et al.* 2015), but a GQL analysis as presented here would obviously also be of considerable interest, with the separation into different scales then possible in both axial and azimuthal directions. Indeed encouragement for this enterprise is obtained from results for the hydrodynamic rotating Couette problem which indicate that GQL remains an attractive approximation when averaging over two spatial directions (in that case streamwise and spanwise directions).

Acknowledgements

AC was supported by an STFC studentship, RH and ST were supported by STFC Grant No. ST/K000853/1, and BM was supported by NSF Grant No. DMR-1306806.

REFERENCES

- AVILA, M. 2012 Stability and angular-momentum transport of fluid flows between corotating cylinders. *Phys. Rev. Lett.* **108**, 124501.
- BAI, X. N. & STONE, J. M. 2014 Magnetic flux concentration and zonal flows in magnetorotational instability turbulence. *Astrophys. J.* **796**, 31.
- BALBUS, S. A. & HAWLEY, J. F. 1991 A powerful local shear instability in weakly magnetized disks. I-Linear analysis. II-Nonlinear evolution. *Astrophys. J.* **376**, 214–233.
- BOUCHET, F., NARDINI, C. & TANGARIFE, T. 2013 Kinetic theory of jet dynamics in the stochastic barotropic and 2D Navier-Stokes equations. *J. Stat. Phys.* **153**, 572 – 625.
- CONSTANTINOU, N. C., FARRELL, B. F. & IOANNOU, P. J. 2013 Emergence and equilibration of jets in beta-plane turbulence: applications of Stochastic Structural Stability Theory. *J. Atmos. Sci.* **72**, 1689 – 1712.
- FARRELL, B. F. & IOANNOU, P. J. 2007 Structure and spacing of jets in barotropic turbulence. *J. Atmos. Sci.* **64**, 3652–3665.
- FARRELL, B. F. & IOANNOU, P. J. 2008 Formation of jets by baroclinic turbulence. *J. Atmos. Sci.* **65**, 3353.
- FLANAGAN, K., CLARK, M., COLLINS, C., COOPER, C. M., KHALZOV, I. V., WALLACE, J. & FOREST, C.B. 2015 Prospects for observing the magnetorotational instability in the plasma Couette experiment. *J. Plasma Phys.* **81**, 345810401.
- GISSINGER, C., GOODMAN, J. & JI, H. 2012 The role of boundaries in the magnetorotational instability. *Phys. Fluids* **24**, 074109.
- GRESSEL, O. & PESSAH, M. E. 2015 Characterizing the mean-field dynamo in turbulent accretion disks. *Astrophys. J.* **810**, 59.
- GUSEVA, A., WILLIS, A. P., HOLLERBACH, R. & AVILA, M. 2015 Transition to magnetorotational turbulence in Taylor-Couette flow with imposed azimuthal magnetic field. *New J. Phys.* **17**, 093018.
- HOLLERBACH, R. 2008 Spectral solutions of the MHD equations in cylindrical geometry. *Int. J. Pure Appl. Math.* **42** (4), 575.
- HOLLERBACH, R. & FOURNIER, A. 2004 *End-effects in rapidly rotating cylindrical Taylor-Couette flow*, *American Institute of Physics Conference Series*, vol. 733, pp. 114–121. AIP Publishing, arXiv: astro-ph/0506081.
- HOLLERBACH, R. & RÜDIGER, G. 2005 New type of magnetorotational instability in cylindrical Taylor-Couette flow. *Phys. Rev. Lett.* **95** (12), 124501.
- HOLLERBACH, R., TEELUCK, V. & RÜDIGER, G. 2010 Nonaxisymmetric magnetorotational instabilities in cylindrical Taylor-Couette flow. *Phys. Rev. Lett.* **104**, 044502.
- JI, H., GOODMAN, J. & KAGEYAMA, A. 2001 Magnetorotational instability in a rotating liquid metal annulus. *Mon. Not. R. Astron. Soc.* **325**, L1–L5.
- JULIEN, K. & KNOBLOCH, E. 2010 Magnetorotational instability: recent developments. *Phil. Trans. Royal. Soc. A* **368** (1916), 1607–1633.
- KIRILLOV, O. N. & STEFANI, F. 2010 On the relation of standard and helical magnetorotational instability. *Astrophys. J.* **712** (1), 52.
- KIRILLOV, O. N., STEFANI, F. & FUKUMOTO, Y. 2014 Local instabilities in magnetized rotational flows: A short-wavelength approach. *J. Fluid Mech.* **760**, 591–633.
- KNOBLOCH, E. 1996 Symmetry and instability in rotating hydrodynamic and magnetohydrodynamic flows. *Phys. Fluids* **8**, 1446–1454.
- LIU, W., GOODMAN, J., HERRON, I. & JI, H. 2006 Helical magnetorotational instability in magnetized Taylor-Couette flow. *Phys. Rev. E* **74**, 056302.
- MARSTON, J. B., CHINI, G. P. & TOBIAS, S. M. 2016 The generalised quasilinear approximation: Application to zonal jets. *arXiv:1601.06720* .
- MARSTON, J. B., QI, W. & TOBIAS, S. M. 2014 Direct statistical simulation of a jet. *arXiv:1412.0381* .
- MEHEUT, H., FROMANG, S., LESUR, G., JOOS, M. & LONGARETTI, P. Y. 2015 Angular momentum transport and large eddy simulations in magnetorotational turbulence: The small Pm limit. *Astro. & Astrophys.* **579**, A117.
- NORNBERG, M. D., JI, H., SCHARTMAN, E., ROACH, A. & GOODMAN, J. 2010 Observation of magnetocoriolis waves in a liquid metal Taylor-Couette experiment. *Phys. Rev. Lett.* **104** (7), 074501.

- PRIEDE, J. 2011 Inviscid helical magnetorotational instability in cylindrical Taylor-Couette flow. *Phys. Rev. E* **84**, 066314.
- PRIEDE, J., GRANTS, I. & GERBETH, G. 2007 Inductionless magnetorotational instability in a Taylor-Couette flow with a helical magnetic field. *Phys. Rev. E* **75**, 047303.
- ROACH, A. H., SPENCE, E. J., GISSINGER, C., EDLUND, E. M., SLOBODA, P., GOODMAN, J. & JI, H. 2012 Observation of a free-Shercliff-layer instability in cylindrical geometry. *Phys. Rev. Lett.* **108**, 154502.
- RÜDIGER, G., HOLLERBACH, R., STEFANI, F., GUNDRUM, T., GERBETH, G. & ROSNER, R. 2006 The traveling-wave MRI in cylindrical Taylor-Couette flow: comparing wavelengths and speeds in theory and experiment. *Astrophys. J. Lett.* **649** (2), L145.
- RÜDIGER, G. & ZHANG, Y. 2001 MHD instability in differentially-rotating cylindrical flows. *Astro. & Astrophys.* **378** (1), 302–308.
- SCHARTMAN, E., JI, H. & BURIN, M. J. 2009 Development of a Couette-Taylor flow device with active minimization of secondary circulation. *Rev. Sci. Instrum.* **80**, 024501.
- SEILMAYER, M., GALINDO, V., GERBETH, G., GUNDRUM, T., STEFANI, F., GELLERT, M., RÜDIGER, G., SCHULTZ, M. & HOLLERBACH, R. 2014 Experimental evidence for nonaxisymmetric magnetorotational instability in a rotating liquid metal exposed to an azimuthal magnetic field. *Phys. Rev. Lett.* **113**, 024505.
- SQUIRE, J. & BHATTACHARJEE, A. 2015 Statistical simulation of the magnetorotational dynamo. *Phys. Rev. Lett.* **114** (8), 085002.
- SRINIVASAN, K. & YOUNG, W. R. 2012 Zonostrophic instability. *J. Atmos. Sci.* **69** (5), 1633–1656.
- STEFANI, F., GERBETH, G., GUNDRUM, T., HOLLERBACH, R., PRIEDE, J., RÜDIGER, G. & SZKLARSKI, J. 2009 Helical magnetorotational instability in a Taylor-Couette flow with strongly reduced Ekman pumping. *Phys. Rev. E* **80** (6), 066303.
- SUZUKI, T. K. & INUTSUKA, S. I. 2014 Magnetohydrodynamic simulations of global accretion disks with vertical magnetic fields. *Astrophys. J.* **784**, 121.
- TOBIAS, S. M., DAGON, K. & MARSTON, J. B. 2011 Astrophysical fluid dynamics via direct statistical simulation. *Astrophys. J.* **727** (2), 127.
- TOBIAS, S. M. & MARSTON, J. B. 2013 Direct statistical simulation of out-of-equilibrium jets. *Phys. Rev. Lett.* **110** (10), 104502.
- VELIKHOV, E. P. 1959 Stability of an ideally conducting liquid flowing between rotating cylinders in a magnetic field. *Sov. Phys. JETP* **36**, 995.